J Solid State Electrochem (2010) 14:803–810
DOI 10.1007/s10008-009-0853-y

ORIGINAL PAPER

Electrochemical behavior of passive films on Al–17Si–14Mg (wt.%) alloy in near-neutral solutions

E. E. Coral-Escobar · M. A. Pech-Canul · M. I. Pech-Canul

Received: 5 February 2009 / Revised: 15 April 2009 / Accepted: 20 April 2009 / Published online: 12 May 2009
© Springer-Verlag 2009

Abstract The anodic polarization behavior of alloy Al–17Si–14Mg in borate solutions with and without 0.01 M NaCl was compared to that for pure Al. Results showed that, for the alloy, the passive current density increased but the pitting susceptibility decreased. The first effect was ascribed to a significant electrochemical activity of the Mg_2Si intermetallics and the second to improved stability of the oxide film. X-ray photoelectron spectroscopy analysis of potentiostatically formed passive film on the alloy showed that it consisted of aluminum oxyhydroxide with incorporation of silicon in its elemental and two oxidized states (+3 and +4). Mott–Schottky analysis showed that trivalent silicon ion acted as an n-type dopant in the film. The interrelationship between passive film composition, electronic properties, and pitting behavior has been discussed.

Keywords Pitting susceptibility · Alloying element · Silicon dopant · Electronic properties

E. E. Coral-Escobar · M. A. Pech-Canul (✉)
Departamento de Física Aplicada, Cinvestav-Mérida,
Km. 6 Ant. Carr. a Progreso, AP 73 Cordemex,
Mérida, Yucatan CP 97310, México
e-mail: max@mda.cinvestav.mx

M. I. Pech-Canul
Cinvestav-Saltillo,
Carr. Saltillo-Mty. Km. 13,
Saltillo, Coahuila CP 25900, México

E. E. Coral-Escobar
Grupo de Instrumentación y Metrología Facultad de Ciencias Básicas, Universidad del Atlántico,
Km. 7 Antigua vía a Puerto Colombia,
Barranquilla, Colombia

Introduction

Aluminum alloys have been extensively used in technological applications due to their low density and high strength-to-weight ratio. Efforts to develop new alloys and aluminum matrix composites with high strength-to-weight ratio and increased stiffness continue. For instance, aluminum matrix composites reinforced with high volume fraction SiC particles are attractive for different structural and electronic packaging applications not only due to its low weight but also due to its ease of fabrication and good thermal properties [1]. Among the different methods of fabrication, the pressureless infiltration technique is a promising one for processing high volume fraction SiCp/Al composites; however, inadequate wetting of silicon carbide and the potential attack of SiC by molten aluminum at temperatures above 900 °C (by the interfacial reaction $4Al + 3SiC \rightarrow Al_4C_3 + 3Si$) represent two major drawbacks. Inadequate wetting leads to considerable levels of residual porosity in the composite, and Al_4C_3 is considered a deleterious phase because it causes a degradation of the thermal–mechanical properties of the composites [2, 3] and also a chemical degradation by its reaction with H_2O [2, 4, 5]. Both problems can be overcome by adequately controlling alloy chemistry, processing time and temperature, preform porosity, particle size, etc. [6, 7]. Magnesium and silicon are the most important alloying elements in aluminum alloys that are designed specifically for infiltrating SiC performance. Both elements reduce the melting point and increase the fluidity of molten aluminum. In addition, Mg is a powerful surfactant which improves wetting of SiC, and Si helps to reduce the activity of aluminum at the interface, thus preventing the formation of Al_4C_3. Due to these requirements, typical levels of Si and Mg are generally higher than those for commercial Al–Si–Mg alloys [8].

A previous work of our research group has focused on optimizing the degree of infiltration [7], evaluating mechanical properties [9] and corrosion behavior [10] of Al–Si–Mg/SiCp composites. Ongoing research involves the use of composites prepared with Al–Si–Mg alloys of varying Si/Mg molar ratio, and one of the objectives is to evaluate the corrosion behavior of plain alloys and compare it with that of the composites.

It is generally accepted that the localized corrosion of aluminum alloys starts at weak spots in the air formed or anodic oxide film and, in the case of highly alloyed substrates, such flaws are often associated to second-phase particles or intermetallics [11–13]. During the past decade, several studies have focused on the electrochemical behavior of intermetallic phases. Starting with the contribution from Suter et al. [14, 15], various authors have used microcapillary electrochemical cells to get an insight into the electrochemical behavior of intermetallics in aluminum-based alloys [16–19]. Other authors used local probing techniques such as atomic force microscopy [20–22], scanning Kelvin probe force microscopy [20, 23, 24], and scanning electrochemical microscopy [21, 22, 25] to investigate the influence of material heterogeneities on localized corrosion properties of aluminum alloys. Although the presence of alloying elements has a determining effect in the formation of second phases or intermetallics (and therefore in the electrochemical behavior of the alloy), it also has a significant effect on the properties of the passive film [12, 13, 26] which may become more or less resistant to pitting corrosion. This is due to the possible incorporation of alloying elements into the oxide film [27, 28] or a modification of its acid–base properties [29].

In this work, the electrochemical behavior of passive films on an Al–Si–Mg alloy with a typical composition of the alloys used for infiltration of SiC performance was evaluated. The role of alloying elements in the composition and electrochemical characteristics of the passive films formed in near-neutral solutions has been discussed in relation to the corresponding passive film for high-purity aluminum.

Materials and methods

The Al–Si–Mg alloy was fabricated in an induction furnace adding aluminum, silicon, and magnesium of commercial purity. The chemical composition is shown in Table 1.

Table 1 Chemical composition (in weight percent) of alloy

Si	Mg	Fe	Cu	Mn	Al
17.51	14.44	0.66	0.02	0.11	Balance

Samples of the alloy were embedded in epoxy resin, leaving a rectangular exposed area of approximately 0.8 cm^2. High-purity aluminum (Goodfellow) with a circular cross-section of 0.283 cm^2 was used as a reference material. Before each electrochemical experiment, the surface of the specimens was abraded down to a 1,200-grit SiC paper, rinsed with distilled water, and dried in hot air. For surface characterization, the samples were also polished to mirror finish using aqueous slurries of 1 to 0.05 µm alumina, then were cleaned ultrasonically for 3 min in distilled water and finally dried with hot air.

Microstructural characterization was carried out by scanning electron microscopy (SEM) with energy dispersion X-ray analysis (EDAX) using a Philips XL30 equipment. X-ray photoelectron spectroscopy (XPS) was used to analyze the chemical composition of the potentiostatically formed oxide layer on the alloy surface. A Perkin-Elmer PHI 560 ESCA-SAM system was used. Binding energy (BE) calibration was based on C 1*s* at 284.6 eV.

Electrochemical measurements were performed with a Gamry series G300 potentiostat–galvanostat in a conventional three-electrode cell where the working electrode was the alloy and Al, the reference was a saturated calomel electrode (SCE), and the counter electrode was a Pt sheet. In order to characterize the anodic behavior of the alloy, potentiodynamic tests were carried out at a sweep rate of 0.3 mV s^{-1} in borate solutions pH 8.4 (with and without addition of 0.01 M NaCl) deaerated with N_2 bubbling before and during the test. Passive films for XPS analysis were grown potentiostatically during 2 h at 0.1 V_{SCE} in the borate solution without chlorides.

The electronic behavior of passive films on aluminum and the alloy was investigated in 0.1 M K_2SO_4 solution pH 7.0 using the Mott–Schottky approach. The electrodes were prepolarized at 0.1 V_{SCE} for 1.5 h to attain steady state, corresponding to a nearly constant thickness of the passive layer. Capacitance versus potential results were then obtained by electrochemical impedance measurements using a 10-mV sinusoidal signal at a single frequency of 10 kHz for potentials between −0.7 and 0.55 V_{SCE}. The impedance measurements started at the more negative limit and proceeded by steps of 0.15 V to the upper limit with a hold time of 30 min at each potential for stabilization.

Results and discussion

Microstructural characterization

Figure 1 shows a backscattered electron SEM image of the Al–17Si–14Mg alloy in which the presence of three phases commonly found in Al–Si–Mg casting alloys is evident [30–32]. The corresponding EDX spectra are presented in

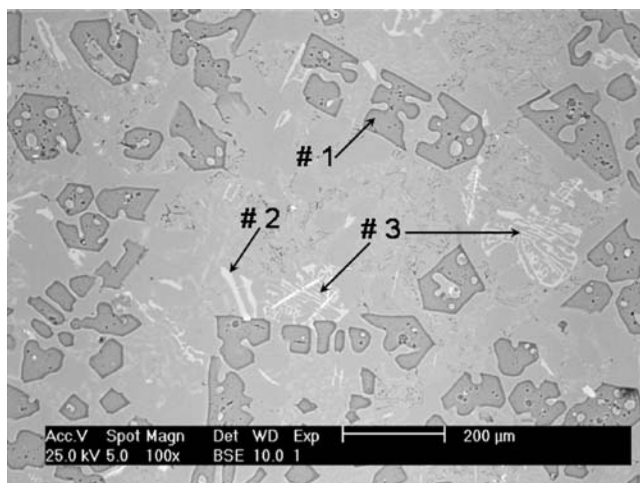

Fig. 1 SEM image of the Al–Si–Mg alloy. The EDAX spectra for the marked phases are presented in Fig. 2

Fig. 2. The dominant phase (phase 1) consists of dark particles, which, according to the EDX analysis and similar microstructural features reported in the literature [20, 31], has been assigned to Mg_2Si. The Mg/Si ratio (in atomic percent) was 1.7:1. This is smaller than the expected (2:1), but it is probably due to the fact that the phase was slightly dissolved during polishing with the aqueous lubricant (which also explains the presence of the oxygen signal). Phase 2 was ascribed to the AlSi eutectic and phase 3 with a typical lamellar or "Chinese-script" structure to the intermetallic compound π-AlFeMgSi [30–32].

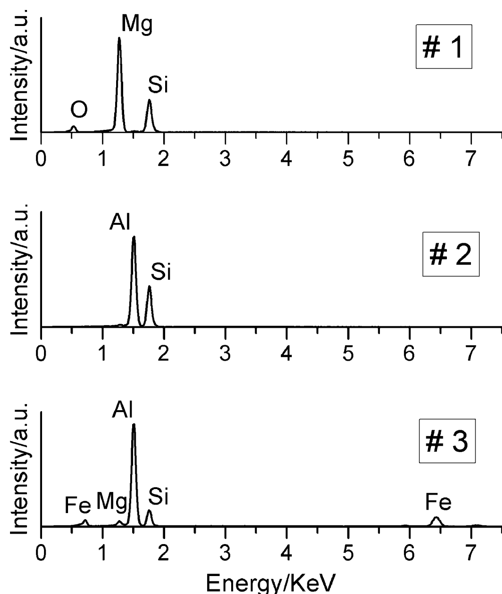

Fig. 2 EDAX spectra for phases *1*, *2*, and *3* in Fig. 1 corresponding to Mg_2Si, the AlSi eutectic, and the π-AlFeMgSi intermetallic, respectively

Electrochemical measurements

Figure 3 shows the anodic polarization curves for the Al–Si–Mg alloy and pure aluminum obtained in borate solutions pH 8.4 with a single sweep rate for Al and two sweep rates for the alloy. It is evident that the Mg content in this alloy has a determining effect on the anodic polarization behavior. Compared to pure Al, the polarization curve for the alloy (at the same sweep rate) is characterized by a much higher anodic activity and the open circuit potential (OCP) is approximately 300 mV more negative. The current density for Al in the passive range is of approximately 10 μA cm^{-2}, while for the alloy is one order of magnitude higher. According to the microstructural characterization, the presence of Mg in the surface of the alloy is by and large in the form of the intermetallic phase Mg_2Si. So, the high anodic activity of the alloy is most likely due to selective dissolution of Mg from this phase. The anodic reactivity of the Mg_2Si intermetallic in aqueous solutions is well-documented in the recent literature [16–20]. It is interesting to observe that the anodic polarization curve for the Al–Si–Mg alloy obtained at 0.3 mV s^{-1} exhibits a small shoulder followed by a slight current decrease at around −0.75 V_{SCE}. At a higher scan rate, the shoulder becomes broader, is shifted to less negative potentials, and involves a net current increase. Such dependence on scan rate suggests that the shoulder might be related to a solid-state mass transport process. This process can be ascribed to dealloying of Mg_2Si and the simultaneous formation of a silicon-rich oxide [18, 20] with some sort of passivation effect (since the magnitude of the current decreases once this oxide is formed). Based on the above discussion, we propose in Fig. 4 a schematic representation of the alloy surface at two different stages of the anodic polarization:

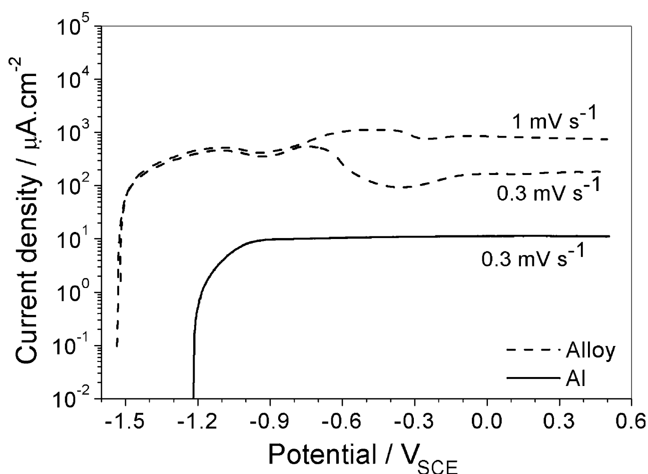

Fig. 3 Anodic polarization curves for Al and the Al–Si–Mg alloy in deaerated borate solutions pH 8.4. For the alloy, results obtained with two sweep rates are presented

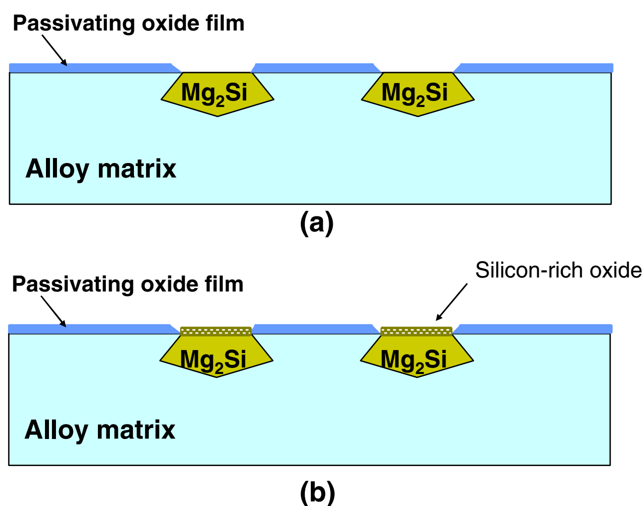

Fig. 4 Schematic representation of the alloy–solution interphase, considering when the anodic reactivity of the Mg_2Si particles is **a** high or **b** low

one when the anodic reactivity of the Mg_2Si particles is high and the other when it is low. Figure 4a corresponds to the initial stage (for potentials below the potential region corresponding to the shoulder) where the Si-rich oxide is absent and Fig. 4b corresponds to the stage when it is present.

Figure 5 shows that, for pure Al, the pitting potential (E_{pit}) is clearly defined (around −0.45 V_{SCE}) by a sharp increase in the current density, while in the case of the alloy E_{pit} is defined by the second current increase in the polarization curve (the first one is associated to the shoulder observed in chloride-free borate solutions). The pitting potential for the Al–Mg–Si alloy exhibited only a slight shift to more noble values; however, the difference between E_{pit} and OCP is wider than that corresponding to pure Al. This suggests that, although its passive current density is large, the pitting susceptibility for the alloy is lower than that for Al. It would be desirable to reduce the current magnitude in the passive region. Thus, future research will be aimed at finding a suitable corrosion inhibitor to suppress the anodic reactivity of the Mg_2Si particles.

The increased pitting resistance of the Al–17Si–14Mg (in weight percent) alloy compared to Al can be related to changes in the properties of the passive film due to the presence of silicon as an alloying element. This assertion is based on the following two reasons: (a) We have recently investigated the effect of Mg alloying addition on dissolution behavior of oxide films [33] and anodic polarization behavior in chloride-containing solutions of Al–Si–Mg alloys [34]. Results of this latter study showed that the pitting potential for Al–10%Si–X%Mg (X=3, 6, 9.5 wt.%) alloys, in borate solutions pH 8.4 with 10 mM NaCl, was about 200 mV more positive than that for pure Al and independent of the Mg content; (b) Unpublished results obtained in our laboratory with Al–12%Si alloy (Goodfellow) have shown, in agreement with observations by other authors [28, 35], that the presence of silicon does indeed increase the resistance to chloride attack. One explanation for the case of Al–Si alloys is that Si is present in the passive film as SiO_2 and, in this form, it alters the acid–base properties of the film, making it more negatively charged (leading to an increase in the pitting resistance) since the isoelectric point of this oxide is less than that for Al_2O_3 [29]. The other possible explanation is that silicon incorporation repairs the film's defects and renders it more stable [28]. Thus, to assess whether silicon is incorporated or not in the passive film of the Al–Si–Mg alloy, an XPS analysis was carried out. The passive films were grown potentiostatically at 0.1 V_{SCE} during 2 h in the borate solution. Next, we present the results of potentiostatic experiments and then the XPS analysis.

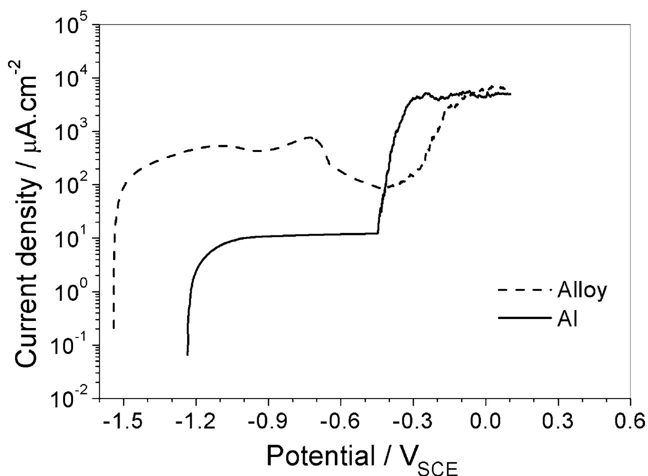

Fig. 5 Anodic polarization curves for Al and the Al–Si–Mg alloy in deaerated borate solutions pH 8.4 containing 0.01 M NaCl

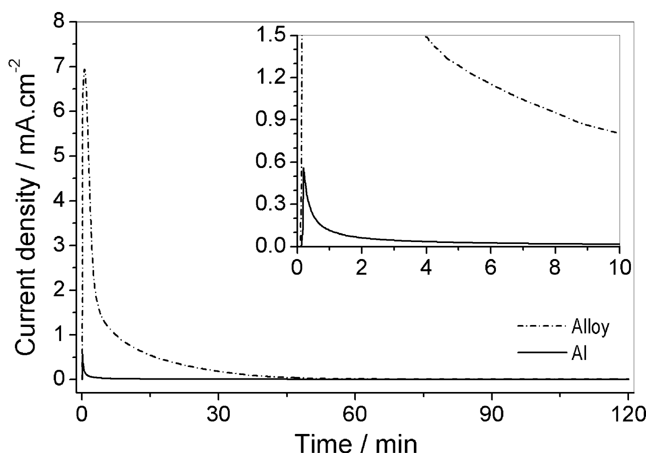

Fig. 6 Potentiostatic transients for Al and the Al–Si–Mg alloy in deaerated borate solutions, pH 8.4, E=0.1 V_{SCE}

Figure 6 shows the typical current transients for Al and the Al–Si–Mg alloy (the inset shows the behavior at short times). The characteristic decrease in anodic current density with time suggests oxide film formation for both samples. For pure Al, the quantity of charge (Q) used for such process was determined by integrating the area under the curve ($i - i_{ss}$) versus time where i_{ss} is the steady-state current density. From the value of Q (=43.6 mC cm^{-2}), the oxide film thickness δ_{ox} was estimated using Faraday's law:

$$\delta_{ox} = \frac{MQ}{zF\rho} \quad (1)$$

where M (101.96 g mol^{-1}) is the oxide molecular mass, ρ (3.2 g cm^{-1}) is the density of Al_2O_3, z (6) the number of electrons used in the process, and F is the Faraday's constant. The value of film thickness determined in this way (24 nm) is in good agreement with the literature [36, 37]. For the alloy, it is evident from Fig. 6 that the charge associated to the current transient is much larger than that for pure Al (about 50 times), suggesting that not all of it was used for oxide film formation. As indicated earlier, part of the current density arises from electrochemical dissolution of intermetallics, and since deconvolution of this contribution is not straightforward then the passive film thickness for the alloy cannot be determined by this method.

XPS surface analysis

Figure 7 shows an XPS survey spectrum for the passive film grown potentiostatically in the Al–Si–Mg alloy. The O 1s, Al 2p, and Si 2p core level principal peaks can be observed. Although the two Mg KLL Auger peaks appear to the left of the C 1s photoelectron peak, the Mg 2p signal is barely discernible. It appears then that, of the two main alloying elements, only silicon shows up in the passive film. In order to elucidate the nature of aluminum oxide and the role of silicon in the film, high-resolution spectra were acquired for O 1s, Al 2p, and Si 2p.

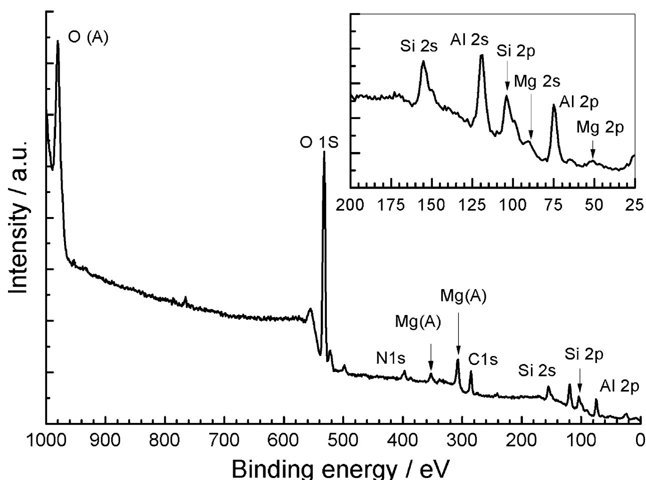

Fig. 7 XPS survey spectra for passive film formed on the Al–Si–Mg alloy after 2 h of potentiostatic treatment at E=0.1 V_{SCE}

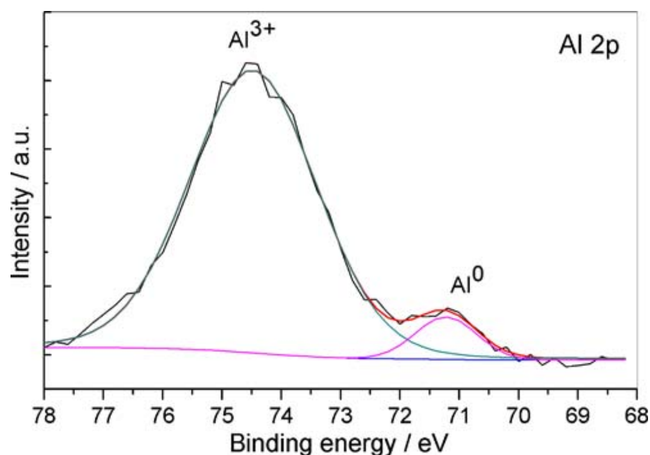

Fig. 8 High-resolution spectrum for Al 2p. Passive film grown as indicated in the caption of Fig. 7

Figure 8 shows the high-resolution spectrum for Al 2p. Deconvolution of this spectrum with the XPSPEAK software [38] suggests that it consists of two peaks, corresponding to aluminum metal (Al^0) and oxidized aluminum (Al^{3+}). Such assignment has been made based on the value of BE for oxidized aluminum and the chemical shift between the two peaks (approximately 3 eV) in agreement with more specialized XPS studies of oxidized aluminum [39, 40].

Figure 9 shows the high-resolution spectrum for Si 2p. Analysis with the XPSPEAK program suggests that it consists of three peaks. The predominant peak at 103.6 eV can be ascribed to the Si^{4+} component, corresponding to SiO_2 [41, 42]. Although the peak corresponding to Si^0 is often reported in the literature to be in the order of 99.5 eV [41–

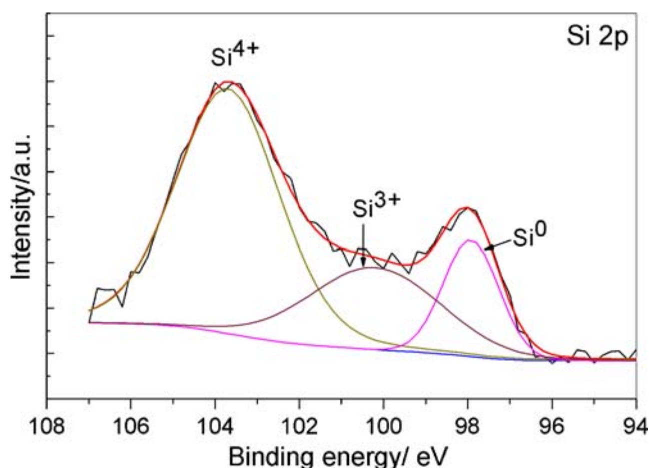

Fig. 9 High-resolution spectrum for Si 2p. Passive film grown as indicated in the caption of Fig. 7

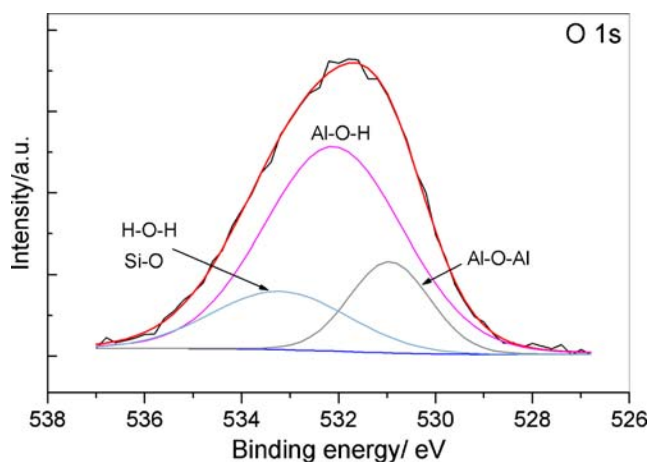

Fig. 10 High-resolution spectrum for O 1*s*. Passive film grown as indicated in the caption of Fig. 7

44], we found that, in this case, it is about 1.5 eV lower. The peak with a BE of 100.2 eV is most likely related to one of the suboxide states (possibly Si^{3+}) in the film [44]. The appearance of this peak might be an indication that the silicon oxide in the passive film is nonstoichiometric.

The high-resolution spectrum for O 1*s* is presented in Fig. 10. Based on more specialized XPS studies on aluminum oxides and oxyhydroxides, this spectrum was decomposed into three components [39, 40]. The first and second peaks (located at 531 and 532.1 eV, respectively) were attributed to the Al–*O*–Al and Al–*O*–H features of aluminum oxyhydroxide. As pointed out by Sherwood and collaborators [27, 39], it is difficult to distinguish among different aluminum oxides by core level XPS since the chemical shifts between them is very small. The third peak (533.2 eV) can be attributed to the contribution from water (H–*O*–H) or to the Si–*O* bond corresponding to the silicon oxide [42, 45].

To sum up, the results of the XPS analysis suggest that the passive film for the Al–Si–Mg alloy consists of an aluminum oxyhydroxide and a certain amount of non-stoichiometric silicon oxide. Its presence might be responsible for the changes in the acid–base properties of the film and also in the electronic properties, as shown below.

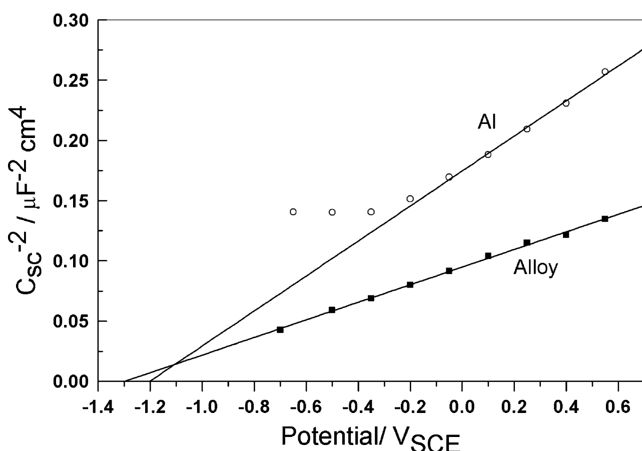

Fig. 11 Mott–Schottky plot for Al and the Al–Si–Mg alloy after the passive film was grown during 2 h at E=0.1 V_{SCE} in a 0.1-M K_2SO_4 solution

Mott–Schottky analysis

It is generally accepted that the resistance of metals and alloys to corrosive attack is related to the solid-state characteristics of the passive film [46, 47]. In particular, for Al and Al alloys, various authors have discussed the correlation between the semiconducting properties of the oxide film and the corrosion resistance [29, 48–51]. For instance, McCafferty [29] reported a dependence of the pitting potential on the flat band potential (E_{fb}) and the isoelectric point of the oxide. Previously, Bockris and Kang [48] had also found a linear relationship between the pitting potential and the potential of zero charge for aluminum and supersaturated aluminum alloys. Most studies have shown that the oxide film on aluminum and its alloys is an n-type semiconductor [29, 48–50].

The analysis of capacitance versus potential data based on the Mott–Schottky theory [52] is the most common method for probing the electronic properties of passive films. According to this theory, the space charge capacitance (C_{sc}) for an n-type semiconductor oxide follows the Mott–Schottky equation:

$$\frac{1}{C_{sc}^2} = \frac{2}{e\varepsilon\varepsilon_0 N_D}\left(E - E_{fb} - \frac{kT}{e}\right) \quad (2)$$

where N_D is the donor concentration, ε is the dielectric constant of the semiconductor, ε_0 is the vacuum permittivity, e is the elementary charge, k is the Boltzmann constant, and T is the temperature. This equation suggests that a plot of $1/C_{sc}^2$ versus E gives a straight line. The point of intersection with the potential axis gives the flat band potential and the slope gives the carrier density.

In this work, values of the space charge capacitance were obtained from the experimentally determined electrode capacitance (C) and the following relationship [47]:

$$\frac{1}{C} = \frac{1}{C_{sc}} + \frac{1}{C_H} \quad (3)$$

corresponding to the series connection between C_{sc} and the Helmholtz layer capacitance C_H. A typical value of C_H= 50 μF cm^{-2} [48] was used in the calculations. Figure 11

Table 2 Results of Mott–Schottky analysis

Sample	E_{fb} (V_{SCE})	N_D (cm^{-3})
Al	−1.23	9.7×10^{19}
Al–Si–Mg	−1.32	1.93×10^{20}

shows the Mott–Schottky plots for aluminum and the Al–Si–Mg alloy obtained in a 0.1-M K_2SO_4 solution. Linear relations with positive slopes indicate that, for both materials, the passive films are n-type semiconductors.

As reported by Schultze and Lohrengel [47], the dielectric constant for Al_2O_3 ranges between 7.5 and 15. In a recent work, Jun et al. [53] showed that Al_2O_3 films deposited by chemical vapor deposition had an initial ε of 7.8 which then increased up to 11.5 after dipping the films in distilled water (i.e., an increase in the dielectric constant due to hydration of the film). Our XPS results described above have shown that the passive film consist of an aluminum oxyhydroxide. Thus, for the estimation of the donor concentration from the slope of the Mott–Schottky plot, a value of $\varepsilon=10$ was used. Values of E_{fb} and N_D obtained from the Mott–Schottky analysis are presented in Table 2. For pure aluminum, the n-type semiconductor behavior of the passive film is most likely due to a predominance of oxygen vacancies. The donor density and the flat band potential are in good agreement with those reported by Bockris and Kang [48].

In the case of the Al–Si–Mg alloy, the flat band potential is about 100 mV more negative than that for passive Al. This is consistent with the finding of Menezes et al. [45] that E_{fb} increases with the tendency of aluminum to undergo pitting. In this case, pure Al is more susceptible to pitting corrosion than the alloy. Concerning the donor concentration, Table 2 shows that N_D for the alloy is about twice that for Al. The XPS results showed that silicon ions are actually found in the passive film and that the ion charge could be +4 or even +3. The fact that the donor density increased suggests that trivalent silicon ion acts as an n-type dopant in the film. Conduction-band electrons were generated by transformation of trivalent silicon (possibly located on an Al lattice site) to the more stable tetravalent state. It is also likely that incorporation of Si species into the Al_2O_3 lattice produced more oxygen vacancies.

Conclusions

The as-cast microstructure of the Al–17Si–14Mg alloy consisted of the Al matrix, the AlSi eutectic, and two intermetallic constituents, Mg_2Si and π-AlFeMgSi. Due to the high levels of Mg and Si, the predominant intermetallic compound was Mg_2Si.

Results of anodic polarization curves in near-neutral borate solutions showed that the Mg content in the Al–Si–Mg alloy had a determining effect (due to the high anodic reactivity of Mg_2Si) leading to a one-order-of-magnitude increase in the passive current density compared to that for Al. Nevertheless, in the presence of chloride ions, the passive film in the alloy exhibited a better pitting resistance compared to that for Al, and this effect was attributed to an improved performance of the oxide film caused by the presence of alloying elements, such as Si.

The XPS analysis of potentiostatically formed passive films in the alloys showed that they consisted of aluminum oxyhydroxide with incorporation of silicon in its elemental and two oxidized states (+3 and +4). On the other hand, Mott–Schottky analysis showed that trivalent silicon ions acted as n-type dopants in the film, leading to an increase in the donor concentration compared to the passive film on pure Al. The silicon ions incorporation also led to a shift in the flat band potential, which, in agreement with other authors, could be correlated with an increase in the pitting resistance compared to that for Al.

Acknowledgements The authors are grateful to Conacyt (National Council of Science and Technology, México) for the financial support under grant no. 51303.Y. E. Coral-Escobar is thankful to Universidad del Atlántico (Colombia) for granting the leave of absence to do doctoral research at Cinvestav-Mérida. The authors also thank Dr. P. Bartolo-Pérez for the useful discussions on surface analytical investigations and to Ms. Dora Huerta and W. Cauich for the technical assistance during the analysis by SEM and XPS, respectively.

References

1. Santhosh Kumar S, Seshu Bai V, Rajasekharan T (2008) J Phys D Appl Phys 41:105403. doi:10.1088/0022-3727/41/10/105403
2. Ren S, He X, Qu X, Humail IS, Li Y (2007) Mater Sci Eng B 138:263. doi:10.1016/j.mseb.2007.01.023
3. Ren S, He X, Qu X, Li Y (2008) J Alloys Compd 455:424. doi:10.1016/j.jallcom.2007.01.127
4. Kosolapova TY (1971) Carbides properties, production and applications. Plenum, New York
5. Park JK, Lucas JP (1997) Scr Mater 37:511. doi:10.1016/S1359-6462(97)00133-4
6. Pech-Canul MI, Katz RN, Makhlouf MM (2000) J Mater Process Technol 108:68. doi:10.1016/S0924-0136(00)00664-6
7. Aguilar-Martínez JA, Pech-Canul MI, Rodriguez-Reyes M, De la Peña JL (2003) Mater Lett 57:4332. doi:10.1016/S0167-577X(03)00323-9
8. Pech-Canul MI, Katz RN, Makhlouf MM (2000) Metall Mater Trans A 31A:265
9. Pech-Canul MI, Ortega-Celaya F, Pech-Canul MA (2006) Mech Compos Mater 42:283. doi:10.1007/s11029-006-0038-z
10. Pech-Canul MI, Escalera-Lozano R, Pech-Canul MA, Rendon-Angeles JC, Lopez-Cuevas J (2007) Mater Corros 58:833. doi:10.1002/maco.200704067
11. Foley RT (1986) Corrosion 42:277
12. Frankel GS (1998) J Electrochem Soc 145:2186. doi:10.1149/1.1838615
13. Szlarska-Smialowska Z (1999) Corros Sci 41:1743. doi:10.1016/S0010-938X(99)00012-8
14. Suter T, Böhni H (1998) Electrochim Acta 43:2843. doi:10.1016/S0013-4686(98)00025-5
15. Suter T, Alkire RC (2001) J Electrochem Soc 148:B36. doi:10.1149/1.1344530
16. Birbilis N, Buchheit RG (2005) J Electrochem Soc 152:B140. doi:10.1149/1.1869984
17. Birbilis N, Buchheit RG (2008) J Electrochem Soc 155:C117. doi:10.1149/1.2829897

18. Wloka J, Bürklin G, Virtanen S (2007) Electrochim Acta 53:2055. doi:10.1016/j.electacta.2007.09.004
19. Wloka J, Virtanen S (2008) Surf Interface Anal 40:1219. doi:10.1002/sia.2868
20. Yasakau KA, Zheludkevich ML, Lamaka SV, Ferreira MGS (2007) Electrochim Acta 52:7651. doi:10.1016/j.electacta.2006.12.072
21. Davoodi A, Pan J, Leygraf C, Norgren S (2006) Appl Surf Sci 252:5499. doi:10.1016/j.apsusc.2005.12.023
22. Davoodi A, Pan J, Leygraf C, Norgren S (2007) Electrochim Acta 52:7697. doi:10.1016/j.electacta.2006.12.073
23. Schmutz P, Frankel GS (1998) J Electrochem Soc 145:2285. doi:10.1149/1.1838633
24. De Wit JHW (2004) Electrochim Acta 49:284
25. Büchler M, Kerimo J, Guillaume F, Smyrl WH (2000) J Electrochem Soc 147:3641. doi:10.1149/1.1393960
26. Elboujdaini M, Ghali E, Barradas MG, Girgis M (1995) J Appl Electrochem 25:412. doi:10.1007/BF00249662
27. Claycomb GD, Sherwood PMA (2002) J Vac Sci Technol A 20:1230. doi:10.1116/1.1479357
28. Rehim SSA, Hassan HH, Amin MA (2004) Corros Sci 46:1921. doi:10.1016/j.corsci.2003.10.016
29. McCafferty E (2003) Corros Sci 45:301. doi:10.1016/S0010-938X(02)00095-1
30. Wang QG, Davidson CJ (2001) J Mater Sci 36:739. doi:10.1023/A:1004801327556
31. Liu YL, Kang SB, Kim HW (1999) Mater Lett 41:267. doi:10.1016/S0167-577X(99)00141-X
32. Yang CY, Lee SL, Lee CK, Lin JC (2005) Mater Chem Phys 93:412. doi:10.1016/j.matchemphys.2005.03.029
33. Pech-Canul MA, Pech-Canul MI, Echeverría M, Montoya-Dávila M (2007) ECS Trans 3:557. doi:10.1149/1.2789257
34. Pech-Canul MA, Pech-Canul MI, Echeverría M (2007) XXII National Congress of the Mexican Electrochemical Society. Pachuca, México, Paper smeq50
35. Amin MA, Hassan HH, Hazzazi OA, Qhatani MM (2008) J Appl Electrochem 38:1589. doi:10.1007/s10800-008-9600-9
36. Lohrengel MM (1995) Ionics 1:393. doi:10.1007/BF02375282
37. Gudić S, Radošević J, Kliškić M (1996) J Appl Electrochem 26:1027. doi:10.1007/BF00242197
38. Kowk RMW (2000) XPSPEAK Version 4.1 XPS peak fitting program. Available at http://www.phy.cuhk.edu.hk/~surface/XPSPEAK
39. Rotole JA, Sherwood PMA (1999) J Vac Sci Technol A 17:1091. doi:10.1116/1.581779
40. Alexander MR, Thompson GE, Beamson G (2000) Surf Interface Anal 29:468. doi:10.1002/1096-9918(200007)29:7<468::AID-SIA890>3.0.CO;2-V
41. Mirji SA (2006) Surf Interface Anal 38:158. doi:10.1002/sia.2309
42. Matsutani T, Asanuma T, Liu C, Kiuchi M, Takeuchi T (2004) Surf Coat Technol 177–178:365. doi:10.1016/j.surfcoat.2003.09.028
43. Green ML, Gusev EP, Degreve R, Garfunkel EL (2001) J Appl Phys 90:2057. doi:10.1063/1.1385803
44. Kim KJ, Park KT, Lee JW (2006) Thin Solid Films 500:356. doi:10.1016/j.tsf.2005.11.042
45. Jeong SH, Kim JK, Kim BS, Shim SH, Lee BT (2004) Vacuum 76:507. doi:10.1016/j.vacuum.2004.06.003
46. Szlarska-Smialowska Z (2002) Corros Sci 44:1143. doi:10.1016/S0010-938X(01)00113-5
47. Schultze JW, Lohrengel MM (2000) Electrochim Acta 45:2499. doi:10.1016/S0013-4686(00)00347-9
48. Bockris JOM, Kang Y (1997) J Solid State Electrochem 1:17. doi:10.1007/s100080050019
49. Fernandes JCS, Picciochi R, Da Cunha Belo M, Moura e Silva T, Ferreira MGS, Fonseca ITE (2004) Electrochim Acta 49:4701. doi:10.1016/j.electacta.2004.05.025
50. Zhang B, Li Y, Wang F (2007) Corros Sci 49:2071. doi:10.1016/j.corsci.2006.11.006
51. Menezes S, Haak R, Hagen G, Kendig M (1989) J Electrochem Soc 136:184. doi:10.1149/1.2097069
52. Morrison SR (1980) Electrochemistry at semiconductor and oxidized metal electrodes. Plenum, New York
53. Jun JH, Kim HJ, Choi DJ (2008) J Ceram Process Res 9:75